



University of HUDDERSFIELD

University of Huddersfield Repository

Stetsyuk, V., Soulopoulos, N., Hardalupas, Y. and Taylor, A. M. K. P.

Experimental assessment of presumed filtered density function models

Original Citation

Stetsyuk, V., Soulopoulos, N., Hardalupas, Y. and Taylor, A. M. K. P. (2015) Experimental assessment of presumed filtered density function models. *Physics of Fluids*, 27 (6). 065107. ISSN 1070-6631

This version is available at <http://eprints.hud.ac.uk/id/eprint/27242/>

The University Repository is a digital collection of the research output of the University, available on Open Access. Copyright and Moral Rights for the items on this site are retained by the individual author and/or other copyright owners. Users may access full items free of charge; copies of full text items generally can be reproduced, displayed or performed and given to third parties in any format or medium for personal research or study, educational or not-for-profit purposes without prior permission or charge, provided:

- The authors, title and full bibliographic details is credited in any copy;
- A hyperlink and/or URL is included for the original metadata page; and
- The content is not changed in any way.

For more information, including our policy and submission procedure, please contact the Repository Team at: E.mailbox@hud.ac.uk.

<http://eprints.hud.ac.uk/>

Experimental assessment of presumed filtered density function models

V. Stetsyuk, N. Soulopoulos, Y. Hardalupas, and A. M. K. P. Taylor

Citation: [Physics of Fluids](#) **27**, 065107 (2015); doi: 10.1063/1.4922169

View online: <http://dx.doi.org/10.1063/1.4922169>

View Table of Contents: <http://scitation.aip.org/content/aip/journal/pof2/27/6?ver=pdfcov>

Published by the [AIP Publishing](#)

Articles you may be interested in

[Comparison of eddy dissipation model and presumed probability density function model for temperature prediction in a non-premixed turbulent methane flame](#)

[AIP Conf. Proc.](#) **1440**, 384 (2012); 10.1063/1.4704240

[Effects of strain rate and curvature on surface density function transport in turbulent premixed flames in the thin reaction zones regime](#)

[Phys. Fluids](#) **17**, 065108 (2005); 10.1063/1.1923047

[Assessment of a flame surface density-based subgrid turbulent combustion model for nonpremixed flames of wood pyrolysis gas](#)

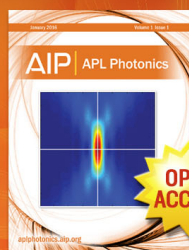
[Phys. Fluids](#) **16**, 3795 (2004); 10.1063/1.1778371

[A subgrid-scale mixing model for large-eddy simulations of turbulent reacting flows using the filtered density function](#)

[Phys. Fluids](#) **15**, 1496 (2003); 10.1063/1.1569920

[A subgrid model for nonlinear functions of a scalar](#)

[Phys. Fluids](#) **13**, 3803 (2001); 10.1063/1.1410385



Launching in 2016!

The future of applied photonics research is here

AIP | APL
Photonics

Experimental assessment of presumed filtered density function models

V. Stetsyuk,^{a)} N. Soulopoulos, Y. Hardalupas, and A. M. K. P. Taylor
Imperial College London, South Kensington Campus, London SW7 2AZ, United Kingdom

(Received 28 January 2015; accepted 26 May 2015; published online 10 June 2015)

Measured filtered density functions (PDFs) as well as assumed beta distribution model of mixture fraction and “subgrid” scale (SGS) scalar variance $\overline{z''^2}$, used typically in large eddy simulations, were studied by analysing experimental data, obtained from two-dimensional planar, laser induced fluorescence measurements in isothermal swirling turbulent flows at a constant Reynolds number of 29 000 for different swirl numbers (0.3, 0.58, and 1.07). Two-dimensional spatial filtering, by using a box filter, was performed in order to obtain the filtered variables, namely, resolved mean and “subgrid” scale scalar variance. These were used as inputs for assumed beta distribution of mixture fraction and top-hat PDF shape estimates. The presumed beta distribution model, top-hat PDF, and the measured filtered density functions were used to integrate a laminar flamelet solution in order to calculate the corresponding resolved temperature. The experimentally measured PDFs varied with the flow swirl number and both axial and radial positions in the flow. The PDFs were unimodal at flow regions with low SGS scalar variance, $\overline{z''^2} < 0.01$, and bimodal at regions with high SGS variance, $\overline{z''^2} > 0.02$. Bimodal PDF could be observed for a filter size of approximately 1.5-2 times the Batchelor scale. Unimodal PDF could be observed for a filter size as large as four times the Batchelor scale under well-mixed conditions. In addition, two common computational models (a gradient assumption and a scale similarity model) for the SGS scalar variance were used with the aim to evaluate their validity through comparison with the experimental data. It was found that the gradient assumption model performed generally better than the scale similarity one. © 2015 Author(s). All article content, except where otherwise noted, is licensed under a Creative Commons Attribution 3.0 Unported License. [<http://dx.doi.org/10.1063/1.4922169>]

I. INTRODUCTION

In Large Eddy Simulations (LESs) of turbulent reacting flows, spatially averaged versions of the equations describing fluid motion are usually solved on a grid, which is “coarse” relative to the smallest scales of fluid motion. In LES, the dynamics of scales that are larger than the filter width (the resolved scales) are captured explicitly, while the effects of the smallest or “subgrid” scales (SGSs) that are not resolved by the filter need to be modelled. The filtered quantity $\overline{f}(x, t)$ (velocity, mixture fraction, etc.) in physical space is simply defined as a convolution of the non-filtered field $f(x', t)$ with a function or convolution kernel, $G_\Delta(x - x')$ as follows:¹

$$\overline{f}(x, t) = \int_{-\infty}^{+\infty} f(x', t) G_\Delta(x - x') dx'. \quad (1)$$

The low-pass spatial filter function G_Δ has characteristic filter width Δ , satisfying $\int G_\Delta(x - x') dx = 1$ and is independent of spatial location. The instantaneous value of any physical

^{a)} Author to whom correspondence should be addressed. Electronic mail: V.Stetsyuk@brighton.ac.uk



quantity f in a turbulent flow can be split into a spatially filtered component (the resolved field) and the fluctuations around the filtered component (the residual field)² $f = \bar{f} + f'$. The spatially filtered component refers to the resolved mixture fraction field \bar{z} , which is computed as a convolution (moving average) of measured mixture fraction fields z with a box filter of various sizes. The effect of the filter size on the resolved mean will be discussed in Sec. III.

A laminar flamelet approach can be used in LES to model reacting flows due to its simplicity and flexibility. This approach is based on a concept of thin, laminar, locally one-dimensional structures (1D, called laminar flamelets) embedded into the turbulent flow field. The main idea behind this approach is to separate the detailed and complex chemistry calculations and the flow fluid dynamics. The laminar flamelet approach reduces the complex chemistry to only two variables, which are the mixture fraction and the scalar dissipation rate. All the dependent variables can then be linked to a single parameter, e.g., the mixture fraction, or to both the mixture fraction and the scalar dissipation rate. The dependent variable is the variable that is computed as a function of the mixture fraction and the scalar dissipation rate.

In order to embed locally one-dimensional laminar flamelets into the turbulent flow, a concept of probability density function (PDF) in the context of Reynolds-Averaged Navier Stokes (RANS) models or filtered density function (FDF, in the context of LES) is used. In adiabatic systems, the flame temperature and the species mass fractions, in general, are parameters of the mixture fraction and the scalar dissipation and, hence, it is possible to calculate in advance so called look up tables (or flamelet solutions) with values of the temperature, species mass fraction, reaction rates, etc., as functions of the mixture fraction. Since in LES, only filtered values of the flow field are known, it is impossible to integrate the flamelet solution in order to obtain the temperature and the species mass fractions because no “subgrid” distribution within the LES computational cells is known.

A general approach to integrate the look-up flamelet tables is based on the solution of the transport equation³ for the filtered density function, which is similar to the transport equation for the RANS-PDF. The success of transported PDF methods^{4,5} in the RANS context promoted the development of the transported FDF concept in the LES context, and the use of FDF-based approaches for subfilter-scale modelling in LES was suggested by Givi.⁶

However, the most simplified and practical modelling approach is based on presumed FDFs, which are usually approximated by beta distribution model or top-hat FDF, parameterized by the first two statistical moments of the mixture fraction, namely, the filtered mixture fraction (the resolved mean) and the “subgrid” scale mixture fraction variance. The validity and applicability of the β -function approximation were investigated by using direct numerical simulation (DNS) data of non-premixed reacting flows.⁷ The results confirm that the β -function provides a good estimate for the FDF of the mixture fraction. However, it was shown^{8,9} that the FDF could substantially deviate from assumed beta distribution model for regions of large “subgrid” scale scalar variance. The presumed FDF can also be based on the so called top-hat function.¹⁰ The β -function and the top-hat function spanning from z_a to z_b are defined as follows:

$$B_Z(z, \bar{z}, \overline{z''^2}) = \frac{z^{a-1}(1-z)^{b-1}}{\int_0^1 z^{a-1}(1-z)^{b-1} dz}, \quad (2)$$

$$\Pi_z(z, \bar{z}, \overline{z''^2}) = \frac{1}{z_b - z_a}, \quad (3)$$

where z is instantaneous mixture fraction, $B_Z(z, \bar{z}, \overline{z''^2})$ is presumed beta density and $\Pi_z(z, \bar{z}, \overline{z''^2})$ is presumed top-hat FDF.

Parameters a and b of the beta distribution model are related to the resolved mixture fraction and the “subgrid” scale mixture fraction variance as follows:

$$a = \bar{z} \left(\frac{\bar{z}(1-\bar{z})}{\overline{z''^2}} - 1 \right), b = (1-\bar{z}) \left(\frac{\bar{z}(1-\bar{z})}{\overline{z''^2}} - 1 \right). \quad (4)$$

Parameters z_a and z_b of the top-hat function are also related to the resolved mixture fraction and its “subgrid” scale scalar variance as follows:

$$l = \sqrt{12\overline{z''^2}}, z_a = \bar{z} - \frac{l}{2}, z_b = \bar{z} + \frac{l}{2}, \quad (5)$$

where $\overline{z''^2}$ is resolved “subgrid” scale scalar variance and \bar{z} is resolved mean computed from measured mixture fraction field.

The filtered mixture fraction is determined by the solution of the transport equations and its variance is usually modelled.^{11,12} If the FDFs are known, the resolved quantities from the laminar flamelet solutions can be computed directly; for instance, if chemistry is assumed to be infinitely fast, local equilibrium is reached and species mass fractions, reaction rates, or red temperature is a function of mixture fraction z only. The mixture fraction z is defined as the ratio of mass of fluid having its origin in the fuel stream to the mass of the stream, in two stream problems. The mixture fraction varies between zero and one, corresponding to no fuel (0) and pure fuel (1),

$$z = \frac{\beta - \beta_{ox,0}}{\beta_{fuel,0} - \beta_{ox,0}}, \quad (6)$$

$$\beta = Y_{fuel} - Y_{ox}/S,$$

$$S = vMW_{ox}/MW_{fuel},$$

where Y_{fuel} is fuel mass fraction, Y_{ox} is oxidizer mass fractions, MW is molar mass, and v is number of moles of oxidizer needed to completely oxidise one mole of fuel.

The spatially averaged quantities are directly obtained by an integration with given filtered density function as follows:

$$\overline{\phi(x,t)} = \int_0^1 \phi(z) B_Z(\bar{z}, \overline{z''^2}) dz, \quad (7)$$

$$\overline{\phi(x,t)} = \int_0^1 \phi(z) \Pi_I(\bar{z}, \overline{z''^2}) dz, \quad (8)$$

where $\overline{\phi(x,t)}$ denotes any spatially filtered variable and $\phi(z)$ is any variable from the laminar flamelet solution (e.g., temperature, species mass fractions, etc.).

The filtered density function f of a scalar ϕ is written as⁸

$$f_\phi(\hat{\phi}; x, t) = \int \delta[\phi(x', t) - \hat{\phi}] G_\Delta(x' - x) dx', \quad (9)$$

where $\hat{\phi}$ is the sample-space variable for ϕ and $\delta[\phi(x', t) - \hat{\phi}]$ is the Dirac delta function.

The filtered density function is in fact a probability density function of a subfilter state, which characterizes the distribution of the scalar within the confines of the filter. The FDF can be constructed from experimentally measured mixture fraction fields or any measured scalars as follows: at a given spatial location, a box filter of known size is applied and the scalar values within the filter confines are extracted. The values are distributed into a number of bins, which are converted into the FDF by counting frequencies in each bin and dividing by a relative bin width (bin width times the number of elements in the dataset),

$$f_\phi(i) = \frac{\hat{\phi}_i}{\Delta_{bin} \times n(\hat{\phi})}, \quad (10)$$

where $\hat{\phi}_i$ is number of mixture fraction values in i histogram bin, Δ_{bin} is bin width used in histogram, and $n(\hat{\phi})$ the total number of mixture fraction values within the confines of the filter.

The shape of the beta density or the top-hat FDF is defined by the first two statistical moments of the mixture fraction. In LES, the resolved mean is available directly from the solution of the filtered transport equations, while a model is needed to approximate the “subgrid” scale scalar

variance. The SGS scalar variance transport equation can in principle be solved, which does not require modelling. However, the SGS scalar variance transport equation, which is regarded as the most accurate in the prediction of the SGS scalar variance, can in some cases result in a non-realistic solution. It was showed that the variance transport equation tended to underpredict the SGS scalar variance due to numerical errors that were related to the numerical approximation of the SGS scalar transport equation.¹³ The SGS scalar variance is important in the scalar dissipation rate modelling and hence an accurate prediction of the SGS scalar variance is paramount.

In this work, we use the “true” measured SGS scalar variance to parametrize the presumed filtered density functions and to calculate a modelled SGS scalar variance to compare with the experimentally measured one. We refer to the measured mixture fraction scalar variance within the box filter as the “true” SGS scalar variance. The SGS scalar variance ($\overline{z''^2}$) can be computed directly from experimentally measured mixture fraction as follows:

$$\begin{aligned}\overline{z''^2} &= \frac{1}{\Delta^2} \sum_{i=1}^{\Delta^2} [z_i - \bar{z}]^2, \\ \bar{z} &= \frac{1}{\Delta^2} \sum_{i=1}^{\Delta^2} z_i,\end{aligned}\quad (11)$$

where Δ is box filter width and z_i is i -value of mixture fraction within the confines of the box filter.

The computation of SGS variance $\overline{z''^2}$ is similar to a low-pass filtering procedure and can be implemented directly. However, computation according to Eq. (11) can be time consuming and non-efficient. In order to increase algorithmic efficiency in computation of SGS variance, it is convenient to rewrite the SGS scalar variance. In order to simplify the implementation of the algorithm, taking into account that the filter function is normalised, i.e., $\int G_\Delta(x - x') dx' = 1$, we obtain as, where the dependence on x and t is omitted for clarity,

$$\overline{z''^2} = \int [z - \bar{z}]^2 G_\Delta(x - x') dx', \quad (12)$$

$$\begin{aligned}\overline{z''^2} &= \int [z^2 - 2z\bar{z} + z\bar{z}]^2 G_\Delta(x - x') dx' = \\ &= \int z^2 G_\Delta(x - x') dx' - 2\bar{z} \int z G_\Delta(x - x') dx' + \bar{z}^2 \int G_\Delta(x - x') dx' = \\ &= \int z^2 G_\Delta(x - x') dx' - \bar{z}^2.\end{aligned}\quad (13)$$

We use Eq. (13) to compute the SGS scalar variance, as the measured squared instantaneous mixture fraction field convolved with a box filter minus the squared resolved mixture fraction field. The two SGS scalar variance models are also briefly introduced here for convenience. The first model is based on a gradient assumption.¹⁴ According to this model, the SGS scalar variance is directly related to the gradient of the resolved scalar field via a modelling constant C_z and the filter width Δ ,

$$\overline{z''^2} = C_z \Delta^2 |\nabla \bar{z}|^2. \quad (14)$$

The second SGS scalar variance model is based on the similarity between large and small scales.¹⁵ The relationship between large and small scales is often approximated by the self-similarity assumption. Under this assumption, the SGS scalar variance can be computed from larger scales by applying the so called test-level filtering. The test-level filtering operation is applied to the resolved field and the SGS scalar variance is computed according to the following formula, where \wedge denotes a test filter, which is often taken to be two times larger than the LES filter.¹⁵

$$\overline{z''^2} = C_{ss} \left(\overline{\bar{z} \cdot \bar{z}} - \widehat{\bar{z}} \cdot \widehat{\bar{z}} \right). \quad (15)$$

The scalar similarity coefficient C_{ss} can be prescribed or defined by using a dynamic procedure, which requires another test filter that must be larger than the test filter used in the model. However,

the assumption of self-similarity is not correct for arbitrary LES filters. It was shown that the base filter (LES filter) and the test filter had to be similar.¹⁶ This means that if, for instance, a box filter is used in the LES simulation, the test filter must be also a box filter. The similarity concept and the similarity assumption model have been evaluated both numerically and experimentally.¹⁷ It was generally found that this model performed better than gradient assumption models.

In addition, we quantify the probability of having bimodal FDF distribution at several locations in the flow. We compute the SGS scalar variance from 1500 instantaneous realisations for a fixed spatial location and fixed filter size and report the results in terms of PDF of the fluctuations of logarithm of the “subgrid” scale scalar variance. The PDF was computed from the logarithm of the instantaneous values of the “subgrid” scale scalar variance minus the mean and normalizing by its standard deviation. If the resulting shape of the PDF of the SGS scalar variance resembles the Gaussian distribution, then the SGS scalar variance will be log-normally distributed.

Also, it is generally expected that if the LES filter size is chosen close to the Batchelor scale, the resulting FDF will be unimodal. However, this statement is not always true and depends on flow dynamics. We demonstrate that the FDF can be bimodal even when the filter size is comparable to the Batchelor scale λ_β . In turn, the FDF can be unimodal when the filter size is 4-5 times larger than the Batchelor length scale,

$$P_{z''^2} = \frac{\ln(\overline{z''^2}) - \overline{\ln(z''^2)}}{\sigma_{\ln(z''^2)}}, \quad (16)$$

where $P_{z''^2}$ is probability density function of SGS scalar variance and $\overline{z''^2}$ is resolved subgrid scale scalar variance.

Even though several experimental attempts to measure filtered density function of mixture fraction in both reacting and non-reacting flows exist,^{8,18,19} no measurements of FDF in swirling flows with low or high swirl number exist to the best of our knowledge. In this paper, we analyse the properties of presumed beta density, top-hat FDF, measured FDF, as well as the PDF of the SGS scalar variance. We evaluate associated dependent variable integration errors that arise from the discrepancy between the measured FDF values and the theoretical presumed FDF output, especially for cases of bimodality. The remaining paper is structured as follows. Section II describes the swirling air flow geometry and the optical instrumentation used to measure the mixture fraction, which is then used to evaluate the presumed FDF modelling methods and the PDF of the SGS scalar variance. Section III describes the results and discusses the findings in terms of the differences between the measurements and the results from the presumed FDFs. The paper ends with a summary of the main conclusions.

II. EXPERIMENTAL SETUP

The burner comprised two concentric pipes with the annulus supplying air and the central pipe delivering air seeded with acetone vapour, which was the measured scalar quantity.^{20,21} The central pipe had an inner diameter $D_f = 15$ mm and an outer diameter of 18 mm, was 0.75 m long and was located concentrically in the outer pipe of inner diameter, $D = 50.8$ mm and centred within it by three locking screws placed 25 mm upstream of the burner exit. The annular flow development section was 0.264 m long. The annular air stream was split into two separately metered streams. One (“tangential air”) passed through a static swirler containing six tangential slots to impart angular momentum. The static swirler was located in a plenum chamber in which the swirling air was combined with the second stream, which delivered “axial air.” Metal plates were installed in the axial and tangential air sections of the plenum chamber to ensure that the axial and tangential air streams were distributed uniformly upstream of the inlets into the annular air supply stream of the burner, where they were combined to control the strength of swirl at the burner exit. The tangential and axial air flow rates were metered by flowmeters after correction to atmospheric pressure and temperature. The axial direction, parallel to the flow propagation, was denoted as “ y ” and the radial direction, perpendicular to the main direction of the flow, as “ x ” (Fig. 1). The swirl number is

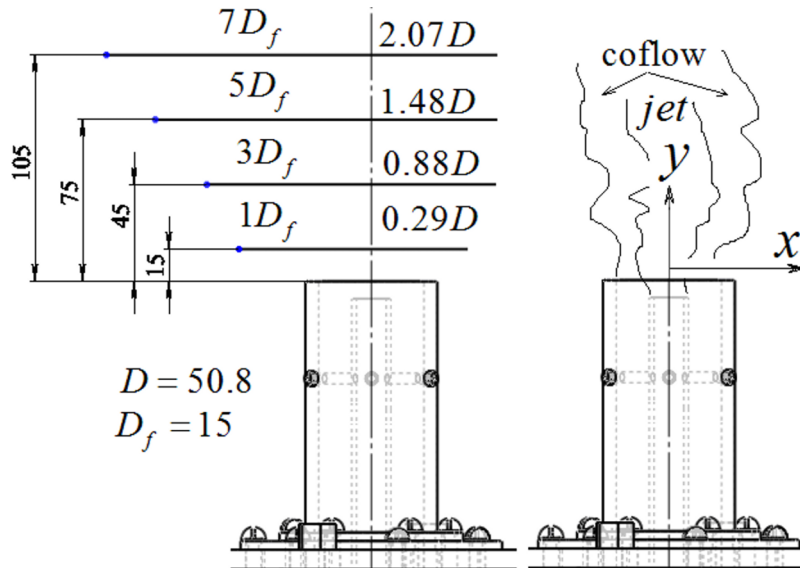


FIG. 1. A schematic view of laser sheet positions during planar laser induced fluorescence (PLIF) measurements (left picture) and flow arrangement (right). Laser sheet positions are shown in absolute values mm, normalized by the fuel pipe internal diameter D_f and by the burner internal diameter D .

defined as follows:²¹

$$S = \frac{2G_{\Theta}}{G_Z D}, \quad (17)$$

$$G_{\Theta} = 2\pi\rho \int_{r=r_i}^R W r U r dr, \quad (18)$$

$$G_Z = 2\pi\rho \int_{r=r_i}^R U U r dr,$$

where S is swirl number, R is radius of the outer pipe, D is diameter of the outer pipe, r_i is radius of the inner pipe, ρ is density, U is axial velocity component, W is tangential velocity component, G_{Θ} is axial flux of angular momentum, and G_Z is axial flux of axial momentum.

The Reynolds numbers in the central (fuel) pipe and in the annular stream were 4000 and 29000, based on the bulk flow velocities of 3.77 m/s and 8.46 m/s, and the diameters of the corresponding streams of 15 mm and 50.8 mm. The Batchelor length scale was in the range of ≈ 300 – $400 \mu\text{m}$ for $S = 0.3$ – 1.07 and was computed from the scalar dissipation spectra as the wavenumber corresponding to 2% of the peak value of the dissipation spectrum.

A Q-switched Nd:YAG frequency-quadrupled 266 nm laser continuum model was used to excite the acetone vapour fluorescence. A single dichroic mirror was used to reflect any laser light at 532 nm and to steer the laser beam from the laser exit port towards the experimental setup and sheet forming optics. The sheet forming optics consisted of a single cylindrical positive lens with focal length of 310 mm. The lens was used to focus the laser beam into a thin waist, with focal point located at the axis of symmetry of the flow. The average laser energy at the test section was 75 mJ/pulse. The actual laser energy fluctuated during experiments from pulse to pulse and the fluctuations were within $\pm 3\%$. Instantaneous corrections of intensity variations of the sheet profile were not performed. The mean laser sheet profile was acquired and used in the image correction procedure, which led to an uncertainty in the mixture fraction measurements of $\pm 5\%$ (when combined with the uncertainty of the reference images).

A double frame CCD camera (LaVision Inc., Imager Intense) was used and was equipped with a Nikkor lens with focal length of 50 mm and f-number of 1.4; a 13 mm extension ring was

also used after the camera lens for tighter focusing. A BG3 bandpass Schott filter was used in front of the camera lens in order to block any remaining 532 nm light that might interfere with the acquired signal. Any scattered light at 266 nm UV wavelength that might come from the test section was blocked by the glass material of the camera lens. The array of the CCD camera was 1376×1040 pixels and the pixel size was $6.45 \mu\text{m}$. The optical magnification was determined by using a calibration target plate and was found to be 0.0263 mm/pixel . The laser sheet thickness was measured as 0.16 mm .

The measured FDFs were computed from the instantaneous images for two box filter sizes of $0.3 (\approx \lambda_\beta)$ and $1.0 \text{ mm} (\approx 3.3\lambda_\beta)$. The smaller filter size was chosen to test an assumption that the LES results should be in better agreement with experiments if the LES filter size Δ is chosen to be as close as possible to the Batchelor length scale. Filter sizes larger than 1 mm were not chosen because bimodality could already be observed.

We measured the SGS scalar variance, the FDF and the probability density function of the SGS scalar variance from nine different spatial locations (Fig. 2) at every laser sheet downstream position (Fig. 1). In order to quantify the probability of having bimodal FDF distributions at specific spatial locations in the flow, the PDF of the SGS scalar variance was computed from 1500 images at all 9 locations.

We have chosen the dependent variable to be a temperature obtained from a laminar flamelet solution as a function of mixture fraction. We used Chemkin-Pro to compute the flame temperature of a methane/air diffusion flame at atmospheric pressure and temperature as a function of mixture fraction. The San Diego reaction mechanism, thermodynamic database, and the transport database from UC San Diego were chosen for this calculation. The laminar flamelet solution, obtained from the planar diffusion flame simulation, was used with the measured FDF, presumed top-hat and beta density, and the associated integration errors were computed as follows:

$$\Delta_\beta = \left| \frac{\overline{T_{fz}} - \overline{T_\beta}}{\overline{T_{fz}}} \right| \cdot 100\%; \Delta_{\Pi_I} = \left| \frac{\overline{T_{fz}} - \overline{T_{\Pi_I}}}{\overline{T_{fz}}} \right| \cdot 100\%, \quad (19)$$

where Δ_β and Δ_{Π_I} are laminar flamelet solution integration errors for presumed beta density and top-hat FDF and $\overline{T_{fz}}$, $\overline{T_\beta}$, and $\overline{T_{\Pi_I}}$ are resolved mean temperatures computed by integration of laminar flamelet solution using measured FDF, presumed beta density, and top-hat FDF, respectively.

A. Effect of experimental noise on FDFs

Filtered density functions of mixture fraction computed from raw mixture fraction images do not usually correspond to the so-called “true” filtered density functions. This is due to digital noise that is always present in the experimental data. The resulting shape of the corresponding filtered function is a combination of “real” mixture fraction distribution within the confines of a filter and the digital noise. Depending on the amount of noise in the experimental data, the finally computed FDF may not reflect the actual mixture fraction distribution. It is, therefore, worth considering both raw and denoised mixture fraction images. The signal-to-noise ratio in the raw images is ≈ 100 and

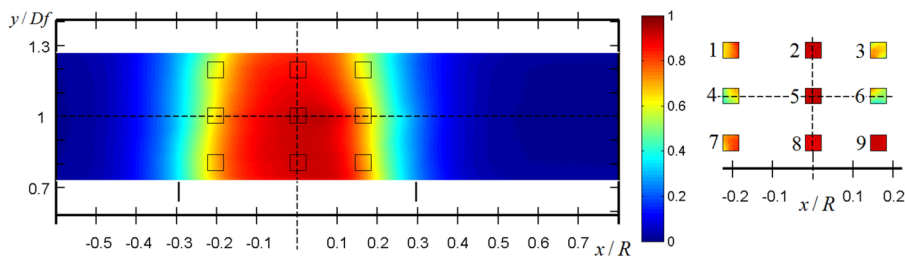


FIG. 2. Spatial locations used to measure the FDF of mixture fraction, the SGS scalar variance, and the PDF of the SGS scalar variance. The time averaged mixture fraction distribution (computed from 1500 realizations) is shown for $y/D_f = 1$ for $S = 0.3$. The associated number for each location is indicated in the right hand side of the figure.

the spatial resolution is $\eta_{MTF@2\%} \approx 300 \mu\text{m}$. We quantified the spatial resolution by measuring the Modulation Transfer Function (MTF)²² using a slanted knife edge method²³ and, as a measure of the resolution, we used the width where the MTF is at 2% of its peak value. We corrected the effects of experimental noise and optical system blurring by using a Wiener filter, which relies on measured signal and noise spectra and on a model for the high-wavenumber decay of the “true” signal spectrum.^{24,25} The result of this signal reconstruction process can be bounded within computed limits and we calculated that in our measurements, depending on the swirl number, the accuracy of the scalar variance measurement is better than 2% and, typically, better than 1%. These errors are, also, within the bounds calculated by modelling the filtering procedure using model spectra and the present turbulent Reynolds number (based on the Taylor length scale) and MTF.²⁶ When we present our results, we also show the effect of the de-noising process on the measured small scale distributions.

III. RESULTS AND DISCUSSIONS

An example of an instantaneous mixture fraction distribution (before any spatial filtering) and the corresponding resolved means, for various filter widths, are shown in Figure 3, at axial distance $y/D_f = 1$ and $S = 0.3$. The resolved mean was computed for three different filter sizes (from top to bottom $\Delta = 1.0, 0.7,$ and 0.5 mm ; $\approx 3.3\lambda_\beta, 2.3\lambda_\beta,$ and $1.7\lambda_\beta$) as a convolution of an original measured mixture fraction field with a box filter. The convolution can be performed, e.g., by using the principle of discrete convolution (or moving average) or in the Fourier domain; we used discrete convolution in the spatial domain. Figure 3 shows that the filtering procedure is equivalent to a low-pass filtering, which results in smoother mixture fraction fields. The filter, in a broad sense, removes smaller scales resulting in a coarser representation of the mixture fraction field.

The subgrid scale scalar variance was computed for four different filter sizes using the bottom image in Figure 3. The measured SGS variance was computed by using Eq. (12) and is shown in Figure 4, which shows that larger box filter corresponds to larger SGS scalar variance. It is also expected that larger SGS scalar variance will change the shape of the measured filtered density functions. In addition, large SGS scalar variance is found in regions where large spatial gradients of the mixture fraction are found. Therefore, it is suggested that the SGS scalar variance (and hence the shape of the FDF) is a function of local mixing regime.

A. Measured filtered density function

In this section, we present measured filtered density functions of the mixture fraction and presumed filtered density functions and we study the effect of the box filter size on the resulting shape of the FDF. An example of filtered density function computation from an experimentally measured mixture fraction field for two different filter sizes is shown in Figure 5. The smallest filter, which was comparable to the Batchelor scale ($\approx 300 \mu\text{m}$) contained almost uniformly distributed mixture fraction values within the confines of the filter. In this case, the FDF would be expected to be unimodal, as it is illustrated in Figure 6. On the other hand, if the filter contains highly segregated mixture fraction values, i.e., with larger fluctuations around the mean, the resulting FDF would be expected to be bimodal (Fig. 6 bottom left).

Figure 7 shows measured FDF for two different filter sizes of 1.0 mm, $\Delta/\lambda_\beta \approx 3.3$, and 0.3 mm, $\Delta/\lambda_\beta \approx 1$, computed for two filter positions (Figure 5). The measured FDF is in fact the probability density function of mixture fraction, such that $\int_0^1 FDF(z) dz = 1$. A bimodal distribution is observable for the largest filter size and an approximately unimodal distribution for the smallest filter size. It should be noted that for fixed filter size, the shape of the FDF will be different as the filter moves along the spatial domain. This is also illustrated in Figure 4, where for fixed filter size, the SGS scalar variance is different and hence, the FDF will also be different.

In addition, we studied the shape of the FDF as a function of the SGS scalar variance. By using trial and error procedures, we experimentally found a threshold SGS scalar variance value above

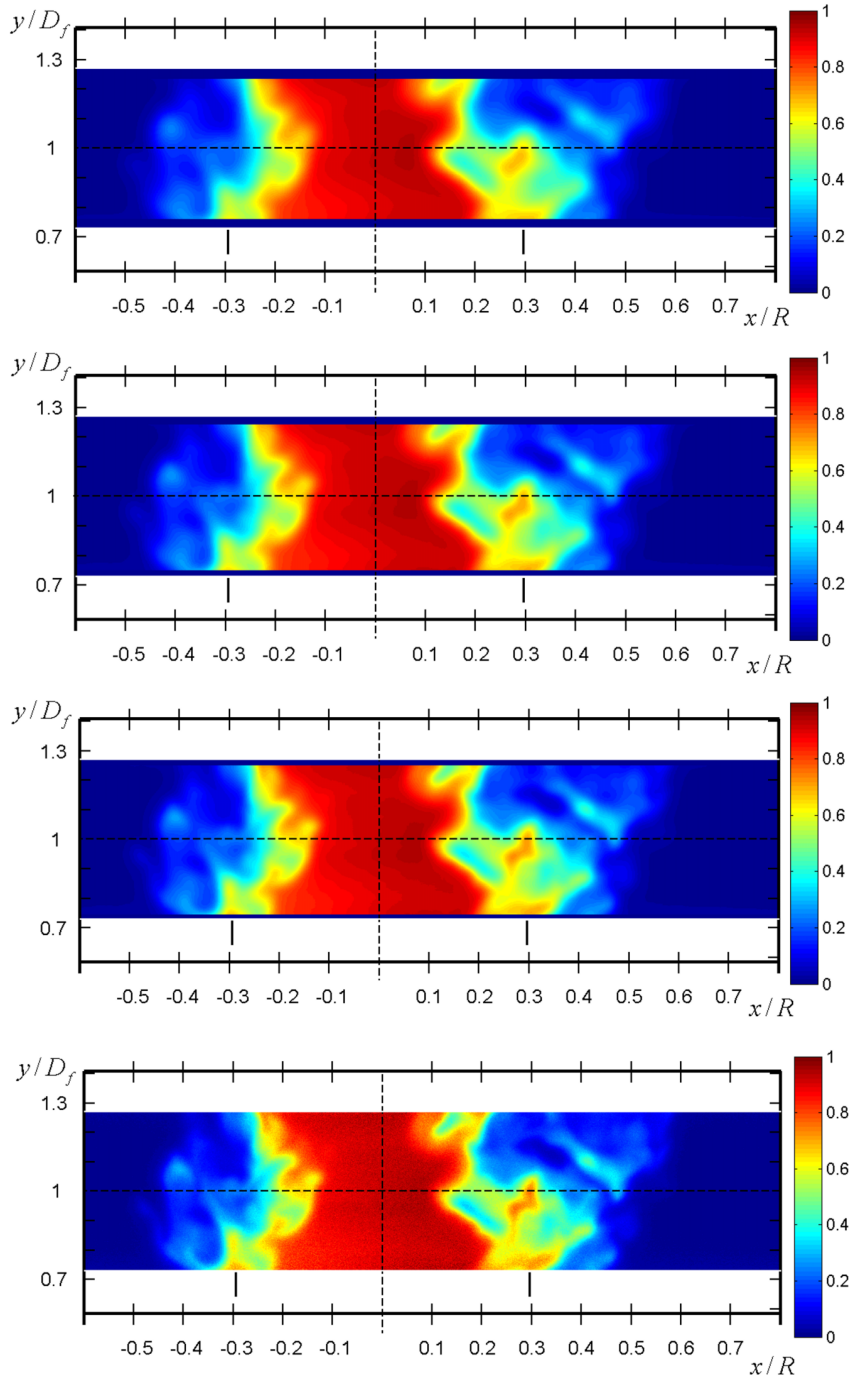


FIG. 3. Measured mixture fraction distribution (raw) with resolution equal to Batchelor scale (the first bottom image) and resolved mean for a range of spatial filter sizes (maximum filter size is 1.0 mm, $\approx 3.3\lambda_\beta$) for $S=0.3$ at $y/D_f=1$. The resolved mean was computed for three different box filters (from top to bottom $\Delta=1.0, 0.7$, and 0.5 mm; $\approx 3.3\lambda_\beta, 2.3\lambda_\beta$, and $1.7\lambda_\beta$). Radial scale was normalised by burner radius R . The position of the edges of the central pipe delivering the acetone vapour jet is shown by the vertical short lines at $\approx \pm 0.3 x/R$.

which the FDF would be bimodal. The threshold was computed to be approximately $\overline{z''^2} = 0.02$. This value was found by plotting the measured FDF as a function of the SGS scalar variance and examining the resulting shape. We, also, define the term “high” and “low” SGS scalar variance as values that are higher or lower than a threshold value, namely, $\overline{z''^2} > 0.02$ and $\overline{z''^2} < 0.02$.

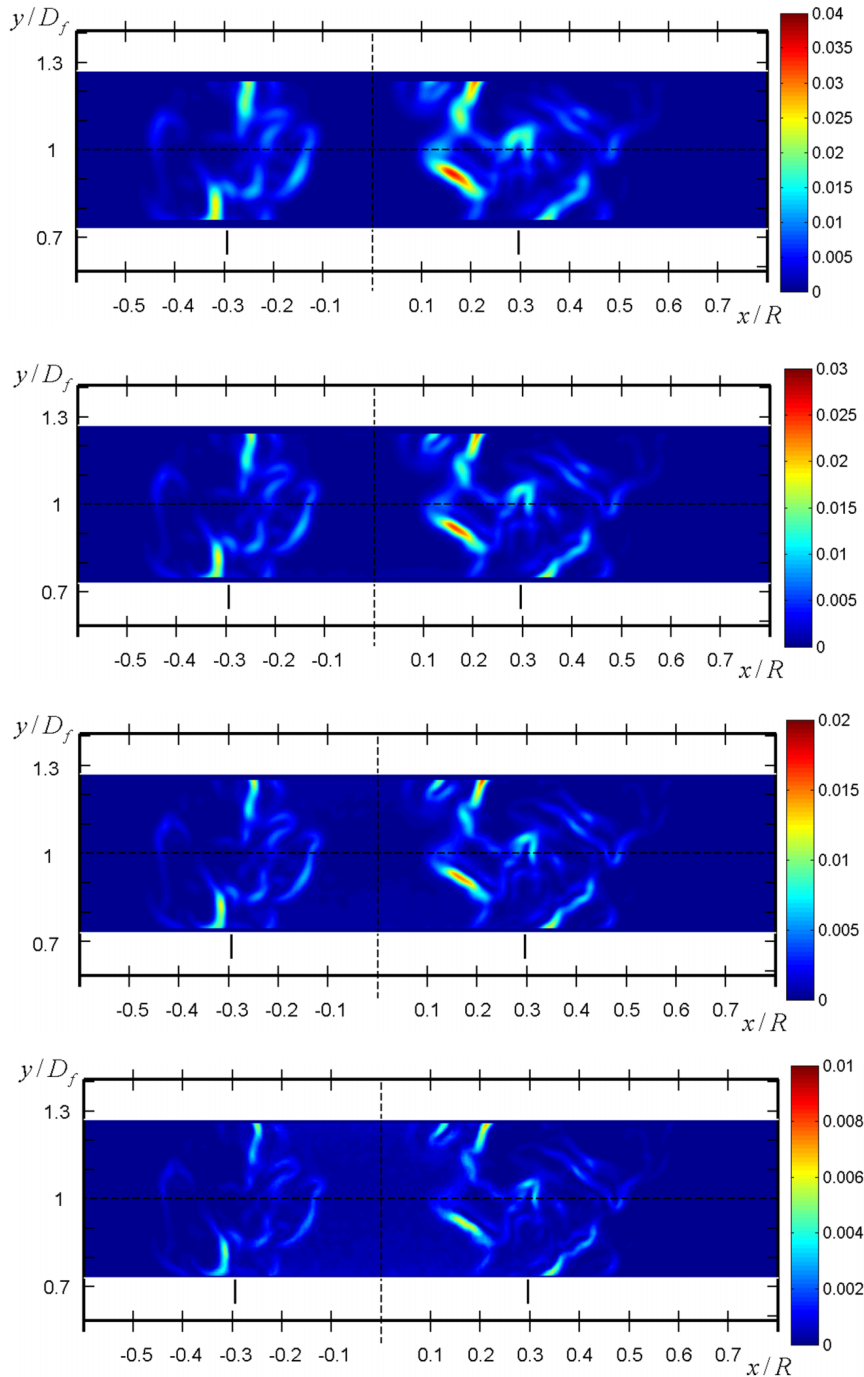


FIG. 4. Measured SGS scalar variance $\overline{z''^2}$ as a function of box filter size (from top to bottom $\Delta = 1.0, 0.7, 0.5$, and 0.3 mm; $\approx 3.3\lambda_\beta, 2.3\lambda_\beta, 1.7\lambda_\beta$, and $1\lambda_\beta$). Radial scale was normalised by burner radius R . The position of the edges of the central pipe delivering the acetone vapour jet is shown by the vertical short lines at $\approx \pm 0.3 x/R$. The SGS scalar variance was computed from the bottom image of Figure 3, which is the measured reference image.

An interesting observation can be seen in Figure 8, which shows measured FDF computed using a filter size of $\Delta/\lambda_\beta = 1.5$; the presumed beta density and top-hat FDF are also shown, which were calculated using the measured resolved mean and measured SGS scalar variance from the same filter. The figure shows that for this small filter, which is comparable to the Batchelor scale, the

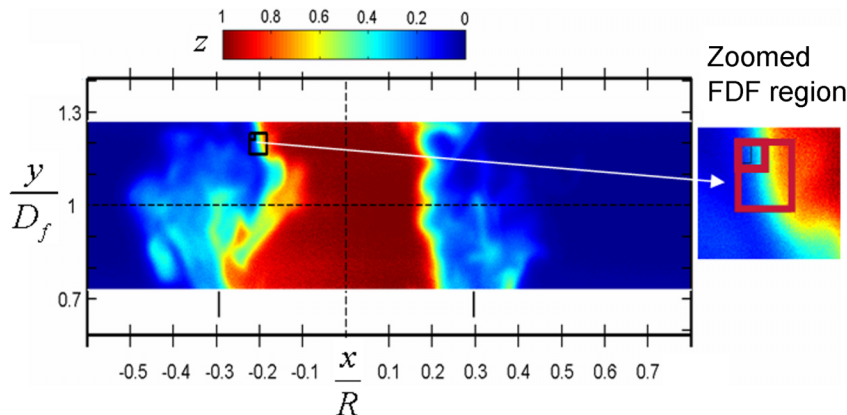


FIG. 5. An example of filtered density function computation from experimentally measured mixture fraction field. The box filter of two different sizes are shown 1.0 mm ($\approx 3.3\lambda_\beta$) and 0.3 mm ($\approx \lambda_\beta$). Instantaneous mixture fraction distribution for $S = 0.3$ at $y/D_f = 1$ is shown as an example of highly non-homogeneous mixture fraction field.

bimodal FDF distribution can still be observed. In fact, Figure 8 demonstrates the so-called “filter overlapped state,” which is schematically illustrated in the cartoon form in Figure 6 (left side).

Calculated presumed beta density and top-hat FDF are also plotted in Figure 8 and in Figure 9. For large SGS variance, neither the beta density nor the top-hat FDF is able to correctly represent the true measured FDF. However, for small SGS variance, the beta density and the top-hat FDF coincide with the measured FDF becoming delta functions and almost indistinguishable.

In addition, the unimodal FDF distribution can be found, e.g., in the jet potential core, where no mixing takes place and hence for any arbitrary filter size, the distribution of the mixture fraction values within the confines of the filter is nearly homogeneous. Similarly, under well-mixed conditions, e.g., at far away distances from the nozzle exit or highly swirling flows, where rapid mixing takes place, the shape of the FDF is likely to be unimodal. Figure 9 shows an example of

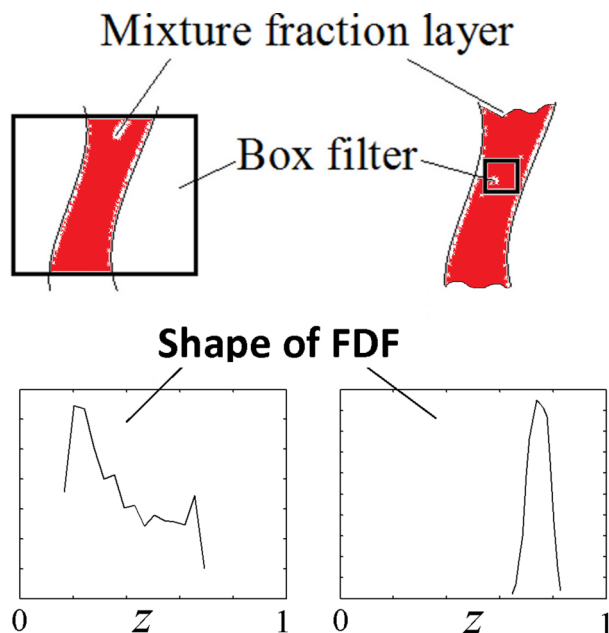


FIG. 6. Schematic illustration of the effect of the box filter size on the FDF. A steep gradient of the mixture fraction is shown as an example; when the mixture fraction field is highly segregated within the filter confines, the FDF is expected to be bimodal.

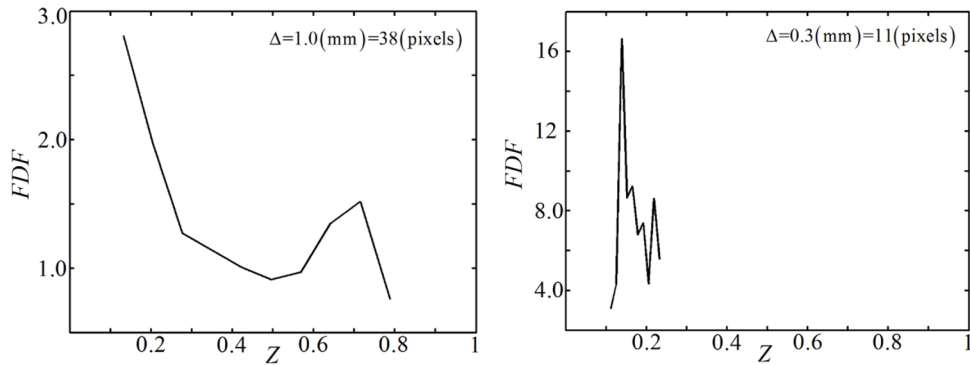


FIG. 7. Measured FDF for two different filter sizes of 1.0 mm, $\Delta/\lambda_\beta \approx 3.3$ (left), and 0.3 mm, $\Delta/\lambda_\beta \approx 1$ (right), computed from filters shown in Figure 5. Plotting range along vertical scale represents probability density function of mixture fraction, such that $\int_0^1 FDF(z) dz = 1$. Vertical scale is not the same in each figure.

measured FDFs from two spatial locations for large filter sizes ($\Delta/\lambda_\beta = 4$) and well-mixed regime at $y/D_f = 7$ for $S = 0.58$. As it can be clearly seen, even for large filter sizes, the shape of the FDF can be unimodal.

The effect of the swirl number cannot be readily assessed from the shape of the FDF because the FDF is by definition computed from the instantaneous realisations. General remarks, which will be supported later by examining the PDF of the SGS scalar variance, are given here as follows. An increase in the level of mixing increases the homogeneity of the flow field, which in turn means that the scalar is locally well-mixed. A well-mixed regime indicates that the SGS scalar variance tends to be low, which results in a unimodal FDF distribution. It was generally found that unimodal distributions were observed at all locations in the flow at $y/D_f = 7$ for $S = 1.07$ and for all filter sizes. This is also consistent with Wang and Tong⁹ where it was pointed out that the conditional FDF was found to be unimodal, and not far from Gaussian, when the SGS variance was small.

The SGS scalar variance is, therefore, the key parameter and is the measure of the level of mixing within one LES cell. It is convenient to relate the measured SGS scalar variance to specific positions in the flow or to operating conditions by considering the probability density function of the SGS scalar variance fluctuations. We report the PDF of the SGS scalar variance, as an example, for one position in the flow (window 3 of Figure 2), according to Eq. (16). A box filter of given size, e.g., 1.0 mm, is fixed at a specific position in the flow and the SGS scalar variance is computed using the filter at every instantaneous realisation. The SGS PDF convergence was checked and we found

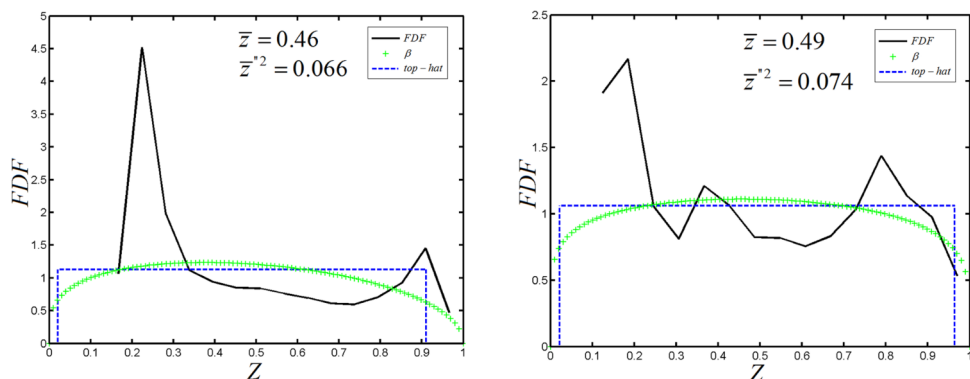


FIG. 8. Measured FDF computed from instantaneous realizations for filter size of $\Delta/\lambda_\beta = 1.5$; beta density (β) and top-hat FDF are also shown, which are calculated from measured resolved mean and measured SGS scalar variance, computed from the same filter.

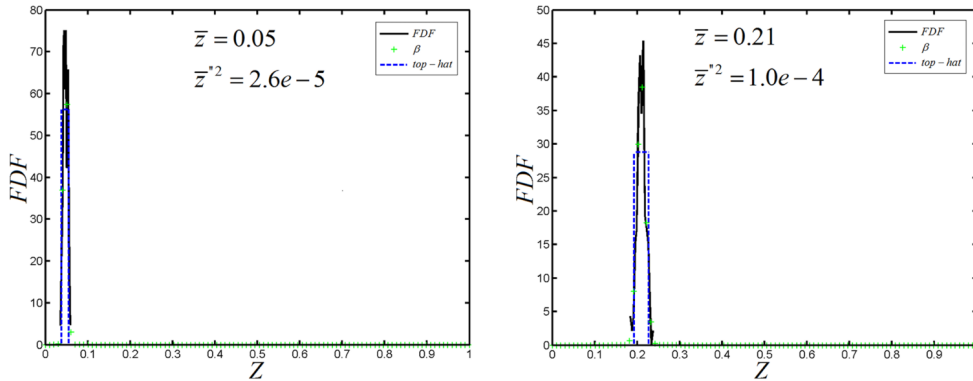


FIG. 9. An example of measured FDFs from two different spatial locations for large filter sizes ($\Delta/\lambda_\beta=4$) and well-mixed regime at $y/D_f=7$ for $S=0.58$; β -FDF and top-hat FDF are shown as green dashed and blue dashed lines, respectively. The beta density and top-hat FDF coincide becoming delta functions and almost indistinguishable.

that the PDF of the SGS scalar variance converged for 1000 realisations rather than the full 1500 realisations.

The measured PDF of the SGS scalar variance for window 3 at $y/D_f=5-7$ for a fixed filter size of 1.0 mm and different swirl numbers is shown in Figure 10, where we note that the PDF of the SGS scalar variance is close to a log-normal distribution. The vertical lines denote threshold positions where $\overline{z'^*2} = 0.02$ for different swirl numbers. As expected, the probability of having bimodal FDF distribution shifts to very low values for the higher swirl numbers of 0.58 and 1.07, which indicated that the distribution is generally unimodal.

An example of a raw and the corresponding denoised mixture fraction image is shown in Figure 11 for $S=1.07$ at $y/D_f=1$, as well as the corresponding FDFs. It is seen that the level of denoising affects the resulting shape of filtered density functions. However, similar trends are generally observed for both raw and denoised FDFs, i.e., bimodality or unimodality. For the smallest filter size, which are comparable with the Batchelor scale, the FDF computed using the denoised mixture fraction distribution can result in unimodal distribution, while the FDF computed using the same filter at the same spatial location at the raw image can result a bimodal distribution. It should be

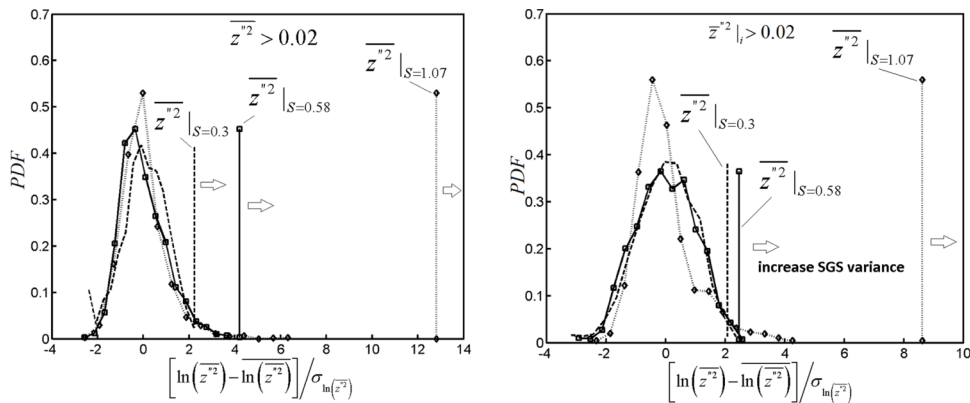


FIG. 10. The measured PDF of the SGS scalar variance computed from 1500 realisations from window 3 at $y/D_f=7$ (left) and the same window at $y/D_f=5$ (right) for a fixed filter size of 1.0 mm and different swirl numbers. The vertical lines denote threshold positions for different swirl numbers, where $\overline{z'^*2} = 0.02$, and arrows indicate increase in the SGS variance. Lines $-\cdot-$, $-\square-$, and $-\diamond-$ denote $S=0.3$, $S=0.58$, and $S=1.07$, respectively. Values along x-axis are plotted according to $\left[\ln(\overline{z'^*2}) - \ln(\overline{z'^*2}) \right] / \sigma_{\ln(\overline{z'^*2})}$.

noted that the experimentally measured FDF in Figure 11 corresponds to the “true” filtered density function, which was corrected for both digital noise and optical system blurring.

Finally, we comment on the integration errors between the temperature computed using the presumed FDF and the corresponding measured FDF. For simplicity and for the sake of brevity, we consider the dependent variable to be the temperature obtained from the laminar flamelet solution. The resolved temperature was computed only for realisations with high SGS scalar variance $\overline{z''^2} > 0.02$, i.e., only when a bimodal FDF distribution was observed. The integration errors were below 1% and a direct correlation between the shape of the presumed beta density and the associated integration error was not found. The weak dependence between the temperatures computed using the presumed FDF and the measured FDF suggests that the SGS scalar variance models, and not the presumed beta density, are perhaps the main source of error in the LES simulations that are based on presumed FDF methods. This is also consistent with Floyd⁷ and Cook and Riley.¹⁵

In addition, we present several integrations of the laminar flamelet solution with the measured FDF, the beta density, and the top-hat FDF in a table form. Table I summarizes several numerical cases for both large and small SGS scalar variances. Large and small SGS variances were obtained from filter sizes in the range of $1.5 < \Delta/\lambda_\beta < 4$, i.e., for high bimodality and unimodality cases. This table reveals that the differences between the integrations with different presumed filtered density functions are not related to resolved subgrid scale variance. The maximum difference between resolved temperature computed from measured FDF (i.e., the true temperature) and the resolved temperatures computed from assumed FDFs is 18.78% for top-hat FDF and 5.1% for beta density. The dimensional value of this difference means error in temperature of 191 K (under-predicted) for top-hat FDF and 33 K (overpredicted) for beta density. For low resolved subgrid scale variance, both beta density and top-hat FDF result in integration errors less than 1.5%. It should be pointed out that high bimodality does not automatically result in large integration errors in resolved variables. Based on these facts, which are supported by Table I, it has been, therefore, suggested that the actual source of error in resolved variables (temperature, species fractions, etc.) could be possibly found in the “subgrid” scale models rather than in presumed FDF methods.

B. Assessment of SGS scalar variance models

We examine here the two common models for the SGS scalar variance: (a) a gradient assumption model with prescribed constant (Eq. (14)) and (b) a scale similarity approach with a prescribed constant (Eq. (15)). Figure 12 shows scatter plots of the SGS scalar variance obtained from an entire single instantaneous image for the filter size of 0.3 mm ($\Delta/\lambda_\beta \approx 1$) and the gradient assumption model predictions performed with the filter of the same size, at $y/D_f = 1$, for $S = 0.3$ and $S = 1.07$.

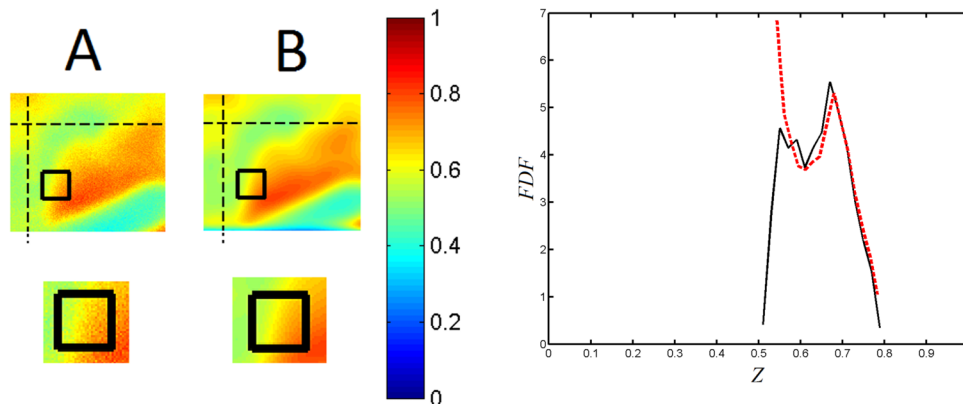


FIG. 11. Left hand side figure shows an example of raw (A) and denoised (B) mixture fraction image. Right hand side figure shows filtered density functions computed from the same filter size and filter location. $S = 1.07$ at $y/D_f = 1$ filter width is 1.0 mm ($\approx 3.3\lambda_\beta$). Solid line on the right hand side figure denotes FDF computed from raw mixture fraction image (A), while dashed line denotes FDF computed from denoised mixture fraction image (B).

TABLE I. Resolved mean temperature obtained by integration of the laminar flamelet solution with measured FDF, presumed beta density, and presumed top-hat FDF. Large and small SGS scalar variances were considered. The associated temperature errors were computed. Large and small SGS variances were obtained from filter sizes in the range of $1.5 < \Delta/\lambda_\beta < 4$.

\bar{z}	\bar{z}''^2	$\bar{T}_{f,z}$, K	\bar{T}_β , K	\bar{T}_{Π_I} , K	Δ_β , %	Δ_{Π_I} , %
0.493	0.0741	993	978	807	1.510	18.731
0.465	0.0659	1017	1019	826	0.197	18.780
0.682	0.0299	654	687	668	5.046	2.141
0.584	0.0265	783	790	841	0.894	7.407
0.430	0.0112	989	1040	1003	5.157	1.415
0.507	$.3 \times 10^{-3}$	852	863	862	1.290	1.174
0.171	1.2×10^{-3}	1594	1611	1604	1.066	0.627
0.440	1.2×10^{-3}	956	966	961	1.046	1.046
0.514	8.8×10^{-4}	842	851	845	1.069	0.356
0.210	1×10^{-4}	1471	1486	1472	1.020	0.021
0.047	2.6×10^{-5}	1816	1837	1802	1.156	0.771

The red straight line is a linear relationship between the experimental and the modelled SGS scalar variances. The model predictions were perfectly correlated with the experimental data because the smallest turbulent length scale was resolved, $\Delta/\lambda_\beta \approx 1$. However, when the swirl number increased, the scatter plot becomes broader (Figure 12 right hand plot) for the smallest filter size, possibly due to the reduction of the local Batchelor scale due to increased turbulence levels. We note that the SGS scalar variance was computed from the entire image (35×9 mm) and not from a specific local area in order to ensure that the comparison contains a sufficient number of measured and computed SGS scalar values.

For a larger filter size of 1.0 mm ($\Delta/\lambda_\beta \approx 3$) (Figure 13), the gradient assumption model deviates from the linear relationship between the experimentally obtained SGS scalar variance and the model output. It is generally observed that the larger filter size affects both the distribution of the SGS scalar variance (SGS deviates from the linear model-experiment relationship) and its magnitude. The spread of the SGS scalar variance increases with increase of the box filter size, especially for higher swirl numbers, because the ratio of Δ/λ_β may increase. However, when the gradient assumption model is employed and when the LES filter size is sufficiently small, $\Delta/\lambda_\beta \approx 1$, the gradient assumption model may be used with a single initially prescribed constant.

The scale similarity model, Figure 14, appears to overestimate or underestimate (depending on the model constant) the variance when compared with the experimental data, even when the smallest filter size is used, so the dynamic procedure to determine the model constant should, also,

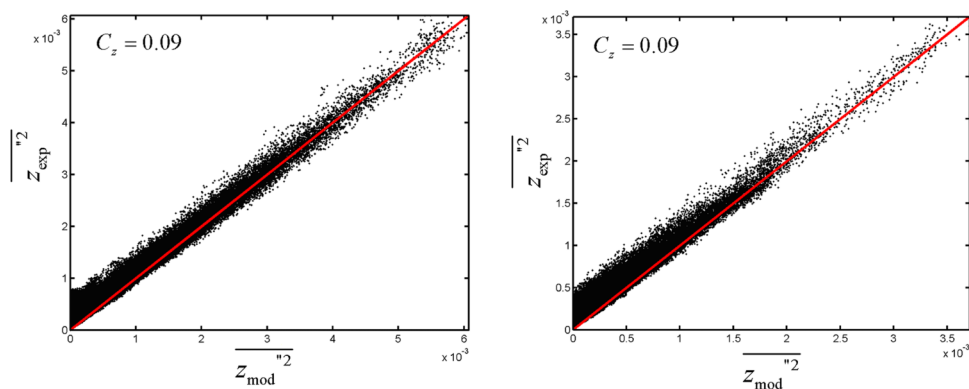


FIG. 12. Scatter plots of the SGS scalar variance computed from an instantaneous image and from the gradient assumption model output at $y/D_f = 1$ for $S = 0.3$ (left) and for $S = 1.07$ (right). Box filter was 0.3 mm, i.e., $\Delta/\lambda_\beta \approx 1$ and model constant C_z was 0.09.

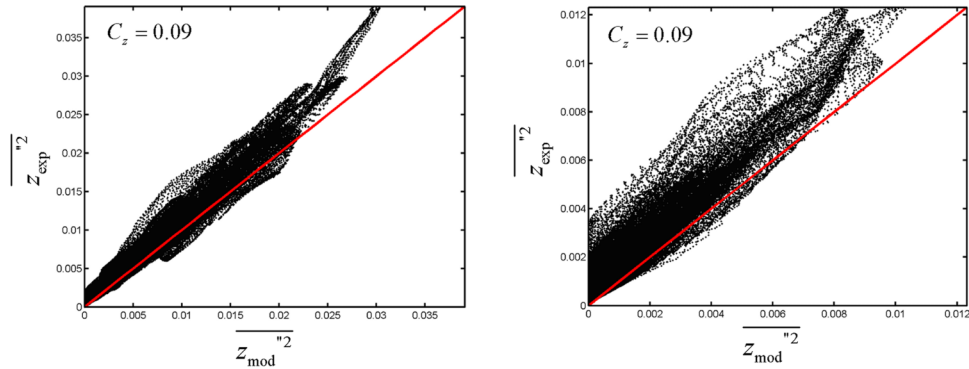


FIG. 13. Scatter plots of the SGS scalar variance computed from an instantaneous image and from the gradient assumption model output at $y/D_f = 1$ for $S = 0.3$ (left) and for $S = 1.07$ (right). Box filter was 1.0 mm, i.e., $\Delta/\lambda_\beta \approx 3$, and model constant C_z was 0.09.

be checked. We used a prescribed constant without employing the dynamic procedure and with the test filter being two times larger than an initial base filter, e.g., if the base filter was 0.3 mm, then the test filter would be 0.6 mm. For the smallest filter size of 0.3 mm, the model constants are the same for both the scale similarity and the gradient assumption models only when $S = 0.3$. Note that V-shaped scatter plot on the right hand side of Figure 14 can be linked to different spatial locations in the image. Since the SGS scalar variance was measured and modelled for the whole image, their relationship may be different for different regions in the flow.

The scale similarity model generally demonstrates an inadequate relationship between the model predictions and the measured data for larger filter size ($\Delta/\lambda_\beta \approx 3$), Figure 15, where an initially prescribed modelling constant is used for the model. The modelling constant that was found to be 0.12 for the filter size of 0.3 mm is different for the larger filter size of 1.0 mm. The discrepancy between the scale similarity model output and the measured SGS scalar variance is larger for larger filter size than in case of the gradient assumption model for the same filter width. In addition to the computational cost due to the additional filtering procedure, the scale similarity model seems to lead to worse estimation of the SGS scalar variance in general.

It should be pointed out that direct extrapolation of results from the present work to reacting flows should be considered carefully. For example, high flame temperature will increase Kolmogorov scale, i.e., the ratio of filter size relative to the fluid-mechanical scales will depend on local temperature. How this affects the FDF is still an open question. In addition, in order to compute

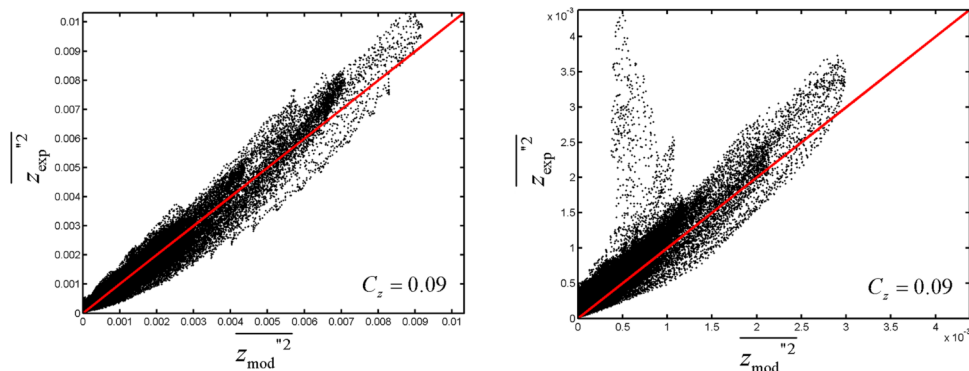


FIG. 14. Scatter plots of the SGS scalar variance computed from an instantaneous image and using the scale similarity model output at $y/D_f = 1$, for $S = 0.3$ (left) and $S = 1.07$ (right). The filter width was 0.3 mm ($\approx \lambda_\beta$) and the model constant was 0.09, as for the gradient assumption model. Note: V-shaped scatter plot on the right hand side can be linked to different spatial locations in the image. Since the SGS scalar variance was measured and modelled for the whole image, their relationship may be different for different regions in the flow.

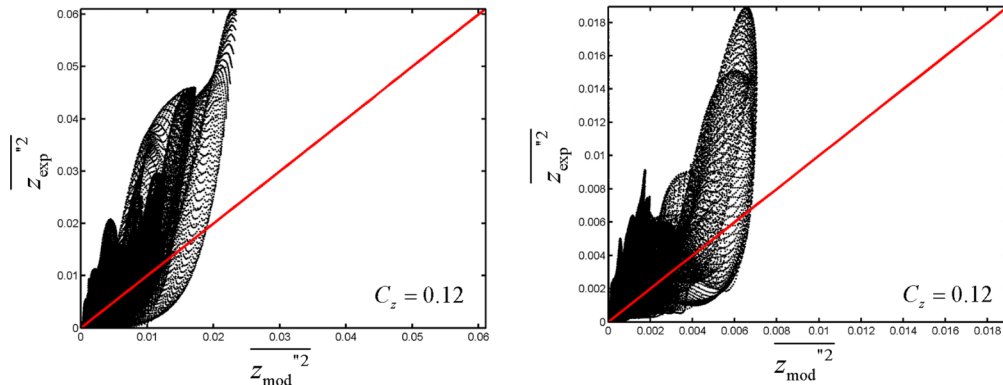


FIG. 15. Scatter plots of the SGS scalar variance computed from an instantaneous image and from the scale similarity model output at $y/D_f = 1$, for $S = 0.3$ (left) and $S = 1.07$ (right). The filter width was 1.0 mm and the model constant was 0.12.

the FDF in reacting flow, mixture fraction distribution must be measured in reacting flows, which is still a non-trivial task, especially in two-dimensional (2D) configurations. Traditionally, point or line (1D) measurements were performed to measure species concentration in reacting flows. The mixture fraction was then computed from measured species concentrations. The authors point out that the measurement of the FDF in isothermal flows is not a substitute for the measurements in reacting flows but rather a step towards understanding of mixing dynamics in swirling flows. In addition, it is expected that the conclusions from this work can be plausible for reacting flows, e.g., mixing and ignition phenomenon. For instance, mixing of reactants in swirling flows and subsequent ignition of “distributed mixture fraction” in a flow recirculation zone. Prior to the flow recirculation zone, there is pure mixing before flame stabilisation, where conclusions from this work may be considered. The two-dimensional nature of the present measurements does not preclude the extension of the conclusions from this work to three-dimensional fields. For different orientations of the measurement plane, there will be different FDF shapes for the same location in the flow. However, the shape of the FDF is related to the subgrid scale mixture fraction distribution and, therefore, conclusions will be plausible for all positions in the flow, regardless the orientation of the measurement plane. Moreover, since FDF is computed from instantaneous realisations, the spatial location of the measured FDF is not important and only the SGS variance is the key variable. The dependence of FDF on SGS variance can be investigated from 2D configurations, which was performed in the present work.

IV. SUMMARY

These experiments focused on the FDFs as well as on the SGS scalar variance. The FDFs were studied by analysing experimental data, obtained from two-dimensional planar, laser induced fluorescence scalar measurements in isothermal swirling turbulent flows. For a filter size, which is comparable to the Batchelor scale, the filtered density functions demonstrated unimodal distributions that were similar to delta functions. The bimodal distributions were observed for filter sizes as small as two times the Batchelor scale and even for $\Delta/\lambda_\beta \approx 1.5$. Higher swirl numbers lead to well-mixed regime, resulting in unimodal FDFs, even for the filter size as large as four times the Batchelor scale. It was also demonstrated that the bimodal distribution of the measured FDF did not automatically introduce errors when integrating the laminar flamelet data. A denoising procedure was also used in order to assess the effect of digital noise on experimentally measured FDFs. It was shown that, even though the shape of the resulting FDF can be quite different, bimodality and unimodality were still observed. Therefore, the above mentioned conclusions are still applicable to raw (non-denoised) data. However, this statement needs to be checked against other denoising techniques as well as for different spatial resolutions and experimental configurations.

The SGS scalar variance was also measured in this work for different filter sizes and swirl numbers. It was demonstrated that the SGS scalar variance increases with box filter size. The PDF of the SGS scalar variance was also presented for a fixed filter size and a spatial location in the flow. It was demonstrated that the probability of having bimodal FDF distribution (high SGS variance) shifted to very low values for the higher swirl numbers of 0.58 and 1.07, which indicated that the distribution was generally unimodal. It was also shown that the PDF of the SGS scalar variance was close to a log-normal distribution. A direct comparison between the measured SGS scalar variance and a modelled variance was provided. Two SGS variance models were chosen, namely, a gradient assumption model and a scale similarity approach, for their simplicity and common use. The discrepancy between the measured SGS scalar variance and the model outputs was negligible with filter width close to the Batchelor scale, for both gradient assumption and scale similarity models. For larger filter size, the gradient assumption model performed better than the scale similarity model for a single value of the modelling constant. Based on the fact that the bimodal FDFs, which were measured in this work, and the corresponding presumed FDF were not correlated in terms of associated laminar flamelet solution integration errors, it has been suggested that the actual source of error in resolved variables (temperature, species fractions, etc.) could possibly be found in the “subgrid” scale models rather than in presumed FDF methods.

ACKNOWLEDGMENTS

This current research was supported by the Alan Howard scholarship for Energy Futures. The authors would also like to acknowledge financial contribution by EPSRC Grant No. GR/R01750/01. Yannis Hardalupas, Nikos Soulopoulos, and Alex Taylor would also like to acknowledge support from EPSRC Grant No. GR/R54767/01.

- ¹ C. Pera, J. Reveillon, L. Vervisch, and P. Domingo, “Modeling subgrid scale mixture fraction variance in LES of evaporating spray,” *Combustion and Flame* **146**, 635 (2006).
- ² D. C. Haworth, “Progress in probability density function methods for turbulent reacting flows,” *Prog. Energy Combust. Sci.* **36**, 168 (2010).
- ³ F. Gao and E. F. O’Brien, “A large-eddy simulation scheme for turbulent reacting flows,” *Phys. Fluids A* **5**, 1282 (1993).
- ⁴ S. B. Pope, “PDF methods for turbulent reactive flows,” *Prog. Energy Combust. Sci.* **11**(2), 119 (1985).
- ⁵ S. B. Pope, “Computations of turbulent combustion: Progress and challenges,” *Proc. Combust. Inst.* **23**(1), 591 (1991).
- ⁶ P. Givi, “Model-free simulations of turbulent reactive flows,” *Prog. Energy Combust. Sci.* **15**(1), 1 (1989).
- ⁷ J. Floyd, A. M. Kempf, A. Kronenburg, and R. H. Ram, “A simple model for the filtered density function for passive scalar combustion LES,” *Combustion Theory and Modelling* **13**(4), 559 (2009).
- ⁸ C. Tong, “Measurements of conserved scalar filtered density function in a turbulent jet,” *Phys. of Fluids* **13**, 2923 (2001).
- ⁹ D. Wang and C. Tong, “Experimental study of velocity-scalar filtered joint density function for LES of turbulent combustion,” *Proc. of the Combustion Institute* **30**(1), 567 (2005).
- ¹⁰ R. Borghi and P. Moreau, “Turbulent combustion in a premixed flow,” *Acta Astronautica* **4**, 321 (1977).
- ¹¹ V. Raman, H. Pitsch, and R. O. Fox, “Hybrid large eddy simulation/Lagrangian filtered density function approach for simulating turbulent combustion,” *Combustion and Flame* **143**, 56 (2005).
- ¹² M. R. H. Sheikhi, T. G. Drozda, P. Givi, F. A. Jaber, and S. B. Pope, “Large eddy simulation of a turbulent nonpremixed piloted methane jet flame (Sandia Flame D),” *Proc. Combust. Inst.* **30**(1), 549 (2005).
- ¹³ C. M. Kaul, V. Raman, G. Balarac, and H. Pitsch, “Numerical errors in the computation of subfilter scalar variance in large eddy simulations,” *Phys. of Fluids* **21**, 55 (2009).
- ¹⁴ C. Pierce and P. Moin, “A dynamic model for subgrid-scale variance and dissipation rate of a conserved scalar,” *Phys. of Fluids* **12**, 3041 (1998).
- ¹⁵ A. W. Cook and J. Riley, “A subgrid model for equilibrium chemistry in turbulent flows,” *Phys. of Fluids* **6**, 2868 (1994).
- ¹⁶ D. Carati and E. V. Eijnden, “On the self-similarity assumption on dynamic models for large eddy simulation,” *Phys. of Fluids* **9**, 2165 (1997).
- ¹⁷ S. Liu, C. Meneveau, and J. Katz, “On the properties of similarity subgrid-scale models as deduced from measurements in a turbulent jet,” *J. of Fluid Mechanics* **275**, 83 (1994).
- ¹⁸ T. G. Drozda, G. Wang, V. Sankaran, J. R. Mayo, J. C. Oefelein, and R. S. Barlow, “Scalar filtered mass density functions in nonpremixed turbulent jet flames,” *Combustion and Flame* **155**, 54 (2008).
- ¹⁹ A. G. Rajagopalan and C. Tong, “Experimental investigation of scalar-scalar dissipation filtered joint density function and its transport equation,” *Phys. of Fluids* **15**, 227 (2003).
- ²⁰ T. F. Dixon, J. S. Truelove, and T. F. Wall, “Aerodynamic studies on swirled coaxial jets from nozzles with divergent quails,” *J. of Fluids Eng.* **105**, 197 (1983).
- ²¹ V. D. Milosavljevic, “Natural gas, kerosene and pulverized fuel fired swirl burners,” Ph.D. thesis (Imperial College of Science Technology and Medicine. Department of Mechanical Engineering, 1993).
- ²² J. W. Goodman, *Introduction to Fourier optics*, 2nd ed. (McGraw-Hill International Editions, 1996).

- ²³ S. E. Reichenbach, S. K. Park, and R. Narayanswamy, "Characterizing digital image acquisition devices," *Opt. Eng.* **30**(2), 170 (1991).
- ²⁴ M. Petrou and P. Bosdogianni, *Image Processing: The Fundamentals* (John Wiley & Sons Ltd., 1999).
- ²⁵ F. J. Krawczynski, B. Renou, L. Danaila, and F. X. Demoulin, "Small-scale measurements in a partially stirred reactor," *Exp. in Fluids* **40**(5), 667 (2005).
- ²⁶ N. Soulopoulos, Y. Hardalupas, and A. M. K. P. Taylor, "Scalar dissipation rate measurements in a starting jet," *Exp. in Fluids* **55**(3), 1 (2014).